DESY 19-102

Relativistic bubble collisions - a closer look

Ryusuke Jinno[a], Thomas Konstandin[a], and Masahiro Takimoto[b]

[a] *DESY, Notkestraße 85, D-22607 Hamburg, Germany*
[b] *Department of Particle Physics and Astrophysics, Weizmann Institute of Science*

Abstract

We study scalar bubble collisions in first-order phase transitions focusing on the relativistic limit. We propose 'trapping equation' which describes the wall behavior after collision, and test it with numerical simulations in several setups. We also examine the energy dynamics after collision and discuss its implications to gravitational wave production.

Contents

1 Introduction

First-order phase transitions lead to a variety of phenomena in the early Universe such as baryogenesis [1], gravitational wave (GW) production [2–7], and magnetogenesis [8], among others. All these phenomena occur during the nucleation of bubbles, their expansion, and collisions. It is therefore important to understand the bubble dynamics in order to predict any possible signal of a first-order phase transition.

The dynamics of bubble expansion is determined by the balance between pressure and friction to the walls: they receive pressure from the supercooled fluid, while friction arises from the particle species which receive masses from the change in the scalar field value. While there are discussions that friction is much more efficient than previously thought [9, 10], it is still important to understand the bubble behavior in a scalar-dominated system, since a scalar-dominated transition is likely to occur when the latent heat is much larger than the plasma energy density (e.g. in near-conformal phase transitions with extreme supercooling [11–29]). If such a transition occurs, the energy released inside cosmological-scale bubbles accumulates mostly on the walls, and the resulting relativistic γ factor is huge (say $\gtrsim 10^{10}$) at the time of collisions. Recent numerical simulations have been performed in Ref. [30–34], often with a focus on oscillons and gravitational wave production. However, simulating bubbles with a large γ factor is on the lattice currently impossible in $3+1$ dimensions.

Given this, the aim of the present work is to develop a method to understand relativistic bubble collisions analytically. We find that, in the relativistic limit, there is a simple governing equation that determines the wall behavior. In particular there is the possibility that after the collision the scalar field bounces back to the symmetric phase and is trapped there. This equation tells us whether the trapping at the false vacuum occurs after collisions. This has huge impact on the GW spectrum, since the GW spectrum takes quite different forms depending on whether the scalar field is damped at the collision point (in which case the envelope approximation [5,6,35,36] should be appropriate) or the walls pass through each other mostly unhindered (in which case the flow approximation [37, 38] should be appropriate). Therefore, our study will help to identify the GW spectrum resulting in scalar-dominated transitions.

The organization of the paper is as follows. In Sec. 2 we first outline our setup and introduce the governing equation, which we call 'trapping equation'. In Sec. 3 we numerically check the validity of this equation with a variety of setups. In Sec. 4 we discuss the application of the trapping equation to $U(1)$ or $SU(2)$ breaking transitions. In Sec. 5 we study the energy localization, which is important in determining the shape of the GW spectrum. Sec. 6 is devoted to conclusions.

2 The scalar dynamics after collisions

The goal of this paper is establish an easy criterion to decide how the scalar field behaves after the collision of two highly-relativistic bubbles. For most parts, we will work in the planar approximation which should be well justified at the first stages of the collision.

The scalar field obeys the Klein-Gordon equations

$$\Box\phi + \frac{dV}{d\phi} = 0\,, \tag{2.1}$$

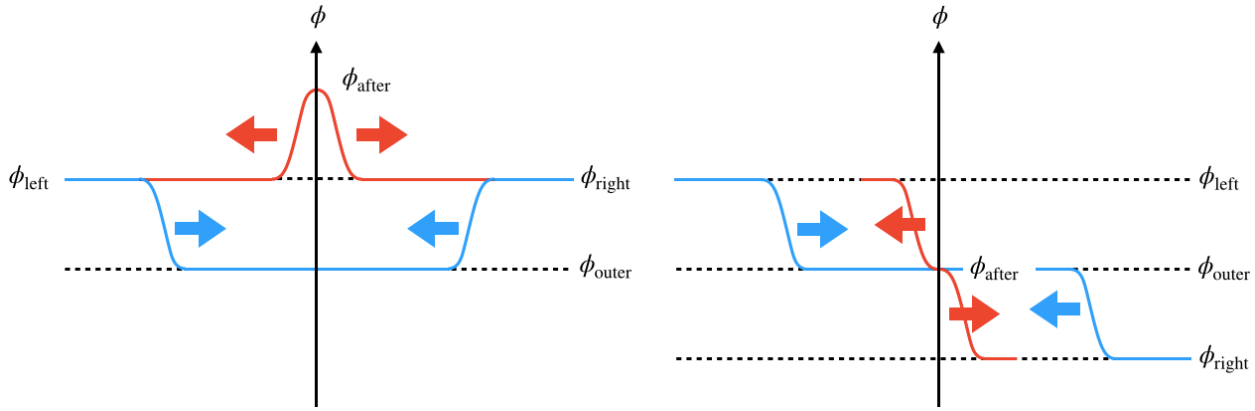

Figure 1: The collision of two solitons (left) and the collision of a soliton and an anti-soliton (right) in a periodic potential. The walls are shown before (blue) and after (red) the collision.

where we neglected all interactions but the self-interactions of the scalar field that are encoded in the scalar potential V. A soliton connects two local minima of the potential and the form of the potential will determine the shape of the soliton while it is accelerating.

One important point is that in the relativistic limit, the kinetic term will dominate the dynamics and the potential is actually irrelevant during the collision. Since the kinetic term only leads to a linear term in the equations of motion, the superposition of two solitons will persist even after collision as long as the solitons collide with a highly-relativistic velocity. The solitons consist of an 'inner' region where the scalar field ϕ has the values ϕ_{left} and ϕ_{right}. The solitons are expanding into an 'outer' region, where the scalar field has a value ϕ_{outer}. As long as the superposition of the solitons persists, the scalar field has to acquire the value

$$\phi_{\text{after}} = \phi_{\text{left}} + \phi_{\text{right}} - \phi_{\text{outer}} \,, \tag{2.2}$$

after the collision. This is exemplified in Fig. 1 where we show the collision of two solitons and the collision of a soliton and an anti-soliton in a periodic potential (in a periodic potential ϕ_{after} is again a minimum of the potential).

However, in the long run and in non-periodic potentials, the scalar field will not pertain the value ϕ_{after} since this is often not a local minimum of the potential. In essence, the scalar field will start rolling down the potential. The boundary conditions are set by the solitons flying apart which induces a $SO(1,1)$ symmetric initial condition and the solution can only depend on the lightfront coordinate $s = \sqrt{t^2 - x^2}$.

If the potential height at the ϕ value after settling down differs from $V(\phi_{\text{left}})$ or $V(\phi_{\text{right}})$, the corresponding wall can decelerate/accelerate which breaks the $SO(1,1)$ symmetry. This will have a large impact on the gravitational wave spectrum created. For almost degenerate potential values, the walls will only use energy through the expansion and the model proposed in Refs. [37,38] is likely to describe the GW production. If there is a large potential difference, the wall is quickly decelerated and the envelope approximation is more likely to describe the GW production [5, 6, 35, 36]. However, on times scales much smaller than the bubble separation, these effects are quite small and the $SO(1,1)$ symmetry is seen in most of our simulations (see Fig. 2).

Under these assumptions the dynamics of the scalar field close to the collision point is

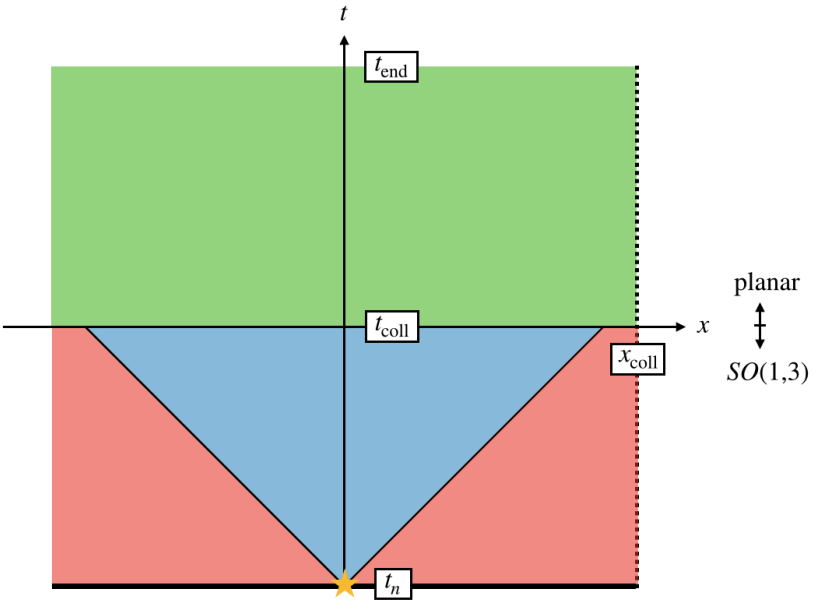

Figure 2: Illustration for our setup. The bubble nucleates at $t = t_n$ at the position of the star. The bounce configuration is located along the thick black line. The scalar field configuration in the spacelike region from the nucleation point (red) is related to the bounce configuration (3.7), while the one in the timelike (blue) region is related to (3.9). The collision time of the bubble $t_{\rm coll}$ is also indicated in the figure. To simulate two colliding bubbles, we impose reflecting boundary conditions at $x = x_{\rm coll}$, which is taken to be slightly larger than $t_{\rm coll} - t_n$. Our interest lies in the evolution of the system in the green region. We take the simulation end $t_{\rm end}$ so that $t_{\rm end} - t_{\rm coll} \approx x_{\rm coll}$ to guarantee that the most relativistic components around $x \simeq x_{\rm coll}$ at $t = t_{\rm coll}$ propagates back to $x \simeq 0$ at $t = t_{\rm end}$. The expanding bubble has $SO(1,3)$ symmetry before $t = t_{\rm coll}$, while we approximate the system to be planar symmetric after collision to simplify the simulation.

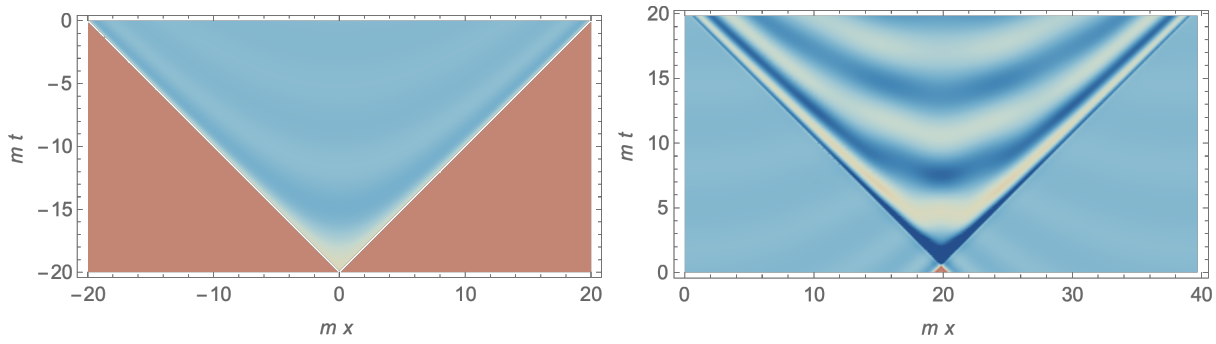

Figure 3: A density plot of the scalar field in a hierarchical model (see Fig. 8). Red and blue regions correspond to the false ($\phi = 0$) and true vacua ($\phi = 1$), respectively. **Left side:** Before $t_{\rm coll}$, corresponding to the red and blue regions in Fig. 2. **Right side:** After $t_{\rm coll}$, corresponding to the green region in Fig. 2.

governed by the 'trapping equation'

$$\partial_s^2\phi + \frac{1}{s}\partial_s\phi + \frac{dV}{d\phi} = 0\,. \tag{2.3}$$

Here, the coordinate s is the $SO(1,1)$ radial direction with the collision point in the origin, $s = \sqrt{t^2 - x^2}$. This equation can be easily solved numerically, which is what we will do in the next section in comparison to scalar field simulations to test our hypothesis.

3 Testing the trapping equation

3.1 Setup and initial conditions

In order to test the trapping equation, we will assume planar symmetry for the colliding bubble walls. For the scalar configuration just before collision, we use initial conditions that are derived from the $3+1$ dimensional setup. Notice that in Secs. 3.2 and 3.3 the potential minima are degenerate and the $3+1$ solutions become the exact soliton profiles in $1+1$ dimensions.

The scalar field fulfills the the equations of motion

$$(\partial_t^2 - \partial_x^2)\phi + \frac{dV}{d\phi} = 0, \tag{3.4}$$

after collision, which assumes planar symmetry. Another important quantity to track is the energy density, which is given by

$$\rho = \frac{1}{2}(\partial_t\phi)^2 + \frac{1}{2}(\partial_x\phi)^2 + V(\phi). \tag{3.5}$$

This will be the relevant indicator how gravitational waves are produced in the present scenario. A more detailed discussion of this topic will be given in section 5.

The next question concerns the initial conditions of the scalar field before collision, i.e. the shape of the soliton during acceleration. Even though our actual simulation is only $1+1$ dimensional, we mainly use the $3+1$ dimensional shape of the soliton. These two configurations can be sizable different due to the friction term in the bounce equation. The evolution of the single bubble configuration after nucleation at $t = t_n$ is as follows:

- In the spacelike region (red) the scalar configuration is related to the bounce configuration $\bar{\phi}$ through $SO(1,3)$ symmetry. That is,

$$\phi(t,r) = \bar{\phi}\left(\sqrt{-(t-t_n)^2 + x^2}\right), \tag{3.6}$$

  where $\bar{\phi}(s = \sqrt{-(t-t_n)^2 + x^2})$ satisfies the bounce equation of motion:

$$\frac{d^2\bar{\phi}}{ds^2} + \frac{3}{s}\frac{d\bar{\phi}}{ds} - \frac{dV}{d\bar{\phi}} = 0. \tag{3.7}$$

- In the timelike region (blue) the scalar configuration is again related through $SO(1,3)$ symmetry

$$\phi(t,x) = \tilde{\phi}\left(\sqrt{(t-t_n)^2 - x^2}\right), \tag{3.8}$$

to the solution $\tilde{\phi}(s = \sqrt{(t-t_n)^2 - x^2})$ of the following equation of motion:

$$\frac{d^2\tilde{\phi}}{ds^2} + \frac{3}{s}\frac{d\tilde{\phi}}{ds} + \frac{dV}{d\tilde{\phi}} = 0. \tag{3.9}$$

In particular, the field performs oscillations around the new local minimum of the potential. The extent of these oscillations is quite different in 3+1 dimensions compared to $1+1$ dimensions and we use the former as mentioned before even though the simulation is lower dimensional.

In the next subsections we will discuss a variety of models and test the trapping equation (2.3). First, we will discuss potentials with degenerate minima and a sizable barrier. In this case, trapping in the old phase is very likely. Next, we modify the potential beyond the new phase (but keep degenerate minima) and study for which parameters the simulation and the trapping equation predict a bounce back into the old phase. This allows for a quantitative test of the trapping equation. Then the opposite case is studied: potentials with a large hierarchy between the two phases and small barriers. First we study the idealized case of an infinitesimal barrier (that only enters in the initial conditions) and then move to more realistic models with and without a Z_2 symmetry. In the following numerical simulations we use the time discretization $\Delta t = 0.1\Delta x$ except for Figs. 12, 22, 23, and 24, in which we use $\Delta t = 0.05\Delta x$. The spatial discretization Δx is chosen depending on the setup.

3.2 Toy model 1: Simple Z_2 potential

We first consider a Z_2-symmetric degenerate potential

$$V = \frac{1}{4}(\phi^2 - v^2)^2. \tag{3.10}$$

As mentioned in Sec. 3.1, the $3+1$ dimensional solutions reduce to the exact soliton profiles in $1+1$ dimensions. The profile is given by

$$\phi(t,x) = \pm v \tanh\left[\frac{\gamma}{\sqrt{2}}\left(x - \sqrt{1 - \frac{1}{\gamma^2}}t\right) + \delta\right], \tag{3.11}$$

with γ being the relativistic γ factor. We initially prepare soliton states according to (3.11) with the value $-v$ in the outer region and evolve the system with reflecting boundary conditions at $x = x_{\rm coll} = 10/v$. According to the trapping equation (2.3), the scalar field bounces back to the minimum at $\phi = -v$ after collision in the large γ limit. We show the time evolution for $\gamma = 5$ (small γ) and 100 (large γ) in Fig. 5. We evolve the system from $t = t_{\rm coll} = 0$ to $t = t_{\rm end} = 10/v$. We take 400γ points for $0 < x < x_{\rm coll}$ so that $\Delta x = 1/40\gamma/v$ for the spatial discretization, and we choose the phase δ so that the argument inside the tanh becomes 5 at the boundary $x = x_{\rm coll}$ at $t = t_{\rm coll}$. It is seen that, for both large and small γ, the scalar field bounces back to $\phi = -v$. This is consistent with the trapping equation (2.3).

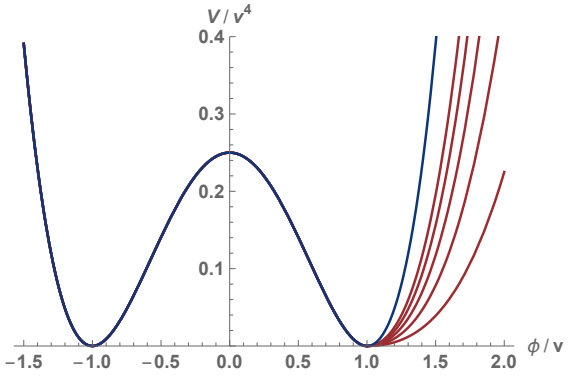

Figure 4: Potential shape of the simple and modified Z_2 model. The top line shows the Z_2-symmetric potential discussed in Sec. 3.2, while the other lines belong to the modified potential in Sec. 3.3 with $\lambda = 0.1, 0.2, 0.3, 0.4$, and 0.5.

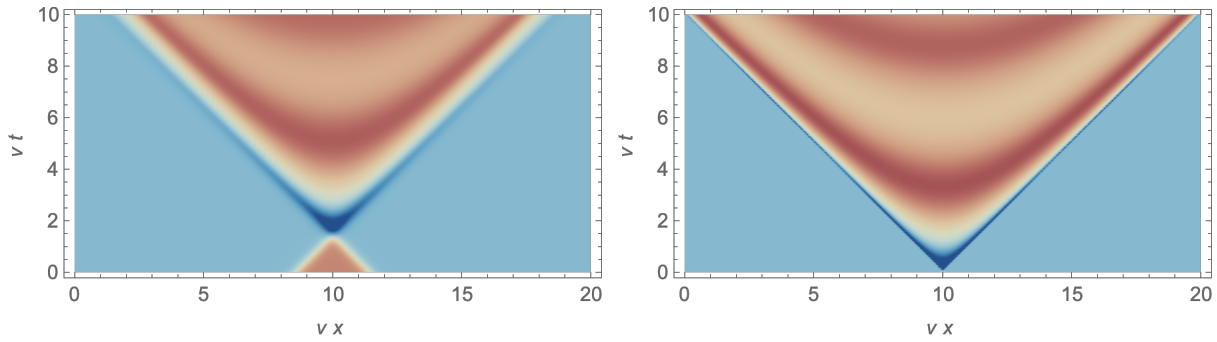

Figure 5: Simple Z_2 potential. Profile of ϕ for the Z_2 potential with a γ factor of 5 (left) and 100 (right). The blue and red regions indicate the positive and negative vacua, respectively.

3.3 Toy model 2: Modified Z_2 potential

We next modify the Z_2-symmetric potential slightly to test the validity of the trapping equation quantitatively:

$$V = \begin{cases} \frac{1}{4}(\phi^2 - v^2)^2 & (\phi \leq v), \\ \frac{\lambda}{4}(\phi^2 - v^2)^2 & (\phi > v). \end{cases} \tag{3.12}$$

Here λ is a free parameter which controls the steepness for $\phi > v$ (see Fig. 4). We solve the same evolution equation as before with the same initial profile. Note that the potential modification for $\phi > v$ does not change the soliton profile. The motivation for making the potential shallower beyond the broken phase is to inhibit that the field is driven back to the symmetric phase after collision. According to the trapping equation (2.3), ϕ settles down to the positive minimum for $\lambda < \lambda_{\rm th} \simeq 0.186$, while it bounces back to the negative minimum for $\lambda > \lambda_{\rm th}$, where $\lambda_{\rm th}$ is a threshold value. Below we will see that this indeed holds in the large γ limit. In Fig. 6, we show the profile of ϕ with $\lambda = 0.1 < \lambda_{\rm th} \simeq 0.186$ (left) and $\lambda = 0.3 > \lambda_{\rm th}$ (right). The blue and red regions indicate that ϕ is in the positive and negative vacua, respectively. We evolve the system from $t = t_{\rm coll} = 0$ to $t = t_{\rm end} = 10/v$ with 200γ points for $0 < x < x_{\rm coll}$. In contrast to Fig. 5, ϕ settles down to the positive minimum for $\lambda = 0.1$, while ϕ bounces back to the negative minimum for $\lambda = 0.3$.

The parametric dependence on the parameters λ and γ is shown in Fig. 7. The red points denote parameters with a bounce back into the negative vacuum ($\phi(t = t_{\rm end}) < 0$), while the blue points denote parameters where ϕ stays in the positive vacuum ($\phi(t = t_{\rm end}) > 0$). The green-dashed line is $\lambda_{\rm th}$ as derived from the trapping equation. The boundary between the blue and red regions coincides very well with $\lambda_{\rm th}$ in the large γ limit.

3.4 Toy model 3: Hierarchical potential

Next let us consider the opposite case to the previous one. We consider a potential where the false vacuum is located at $\phi = 0$ with an infinitesimally small trap. The true vacuum is located at $\phi = v$, and the potential shape around it is quadratic. Thus

$$V \simeq \frac{1}{2}m^2(\phi - v)^2, \tag{3.13}$$

up to small effects very close to the symmetric phase. As mentioned in Sec. 3.1, we regard the system to be $3+1$ dimensional until collision (i.e. spherical), while approximate it to be $1+1$ (i.e. planar) when we calculate collision dynamics.

For a quadratic potential, the initial conditions (3.7) and (3.9) are solved analytically

$$\tilde{\phi}(s) = v\left[1 - \frac{2J_1(ms)}{ms}\right], \tag{3.14}$$

where J_1 is the Bessel function. Therefore, the scalar configuration is given by

$$\phi(t, x) = v\left[1 - \frac{2J_1\left(m\sqrt{(t - t_n)^2 - x^2}\right)}{m\sqrt{(t - t_n)^2 - x^2}}\right]. \tag{3.15}$$

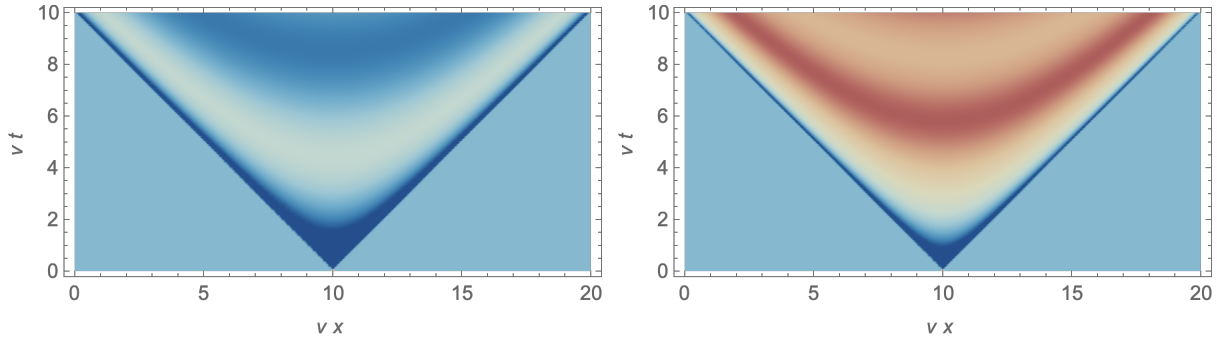

Figure 6: Profile of ϕ for the modified Z_2 potential with a γ factor of 100 with $\lambda = 0.1$ ($< \lambda_{\rm th} \simeq 0.186$, left) and $\lambda = 0.3$ ($> \lambda_{\rm th}$, right). The blue and red regions indicate the positive and negative vacua, respectively. For the former the scalar field does not bounce back to the vacuum at $\phi = -v$ while it does for the latter. Compare with the right panel of Fig. 5.

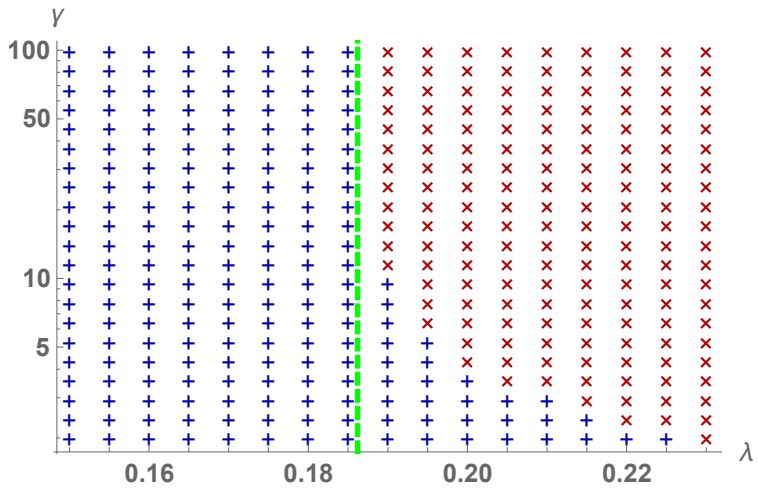

Figure 7: Modified Z_2 potential. The red and blue points are parameter points where $\phi(t = t_{\rm end}) \lessgtr 0$, respectively. The green-dashed line is $\lambda = \lambda_{\rm th} \simeq 0.186$ predicted by Eq. (2.3).

For the collision, we again approximate the walls to be planar. Since the effect of the configuration in the spacelike region is infinitesimally small, we may approximate the configuration at the beginning of the simulation ($t = t_{\rm coll}$) as

$$\phi(t,x)|_{t=t_{\rm coll}} \simeq \begin{cases} v\left[1 - \dfrac{2J_1\left(m\sqrt{(t_{\rm coll}-t_n)^2 - x^2}\right)}{m\sqrt{(t_{\rm coll}-t_n)^2-x^2}}\right] & (0 < x < t_{\rm coll} - t_n), \\ 0 \quad (t_{\rm coll} - t_n < x), \end{cases} \tag{3.16}$$

and also the time derivative is given by

$$\partial_t\phi(t,x)|_{t=t_{\rm coll}} \simeq \begin{cases} v\,\partial_t\left[1 - \dfrac{2J_1\left(m\sqrt{(t_{\rm coll}-t_n)^2 - x^2}\right)}{m\sqrt{(t_{\rm coll}-t_n)^2-x^2}}\right]\Bigg|_{t=t_{\rm coll}} & (0 < x < t_{\rm coll} - t_n), \\ 0 \quad (t_{\rm coll} - t_n < x). \end{cases} \tag{3.17}$$

We then study the time evolution of the system with these initial conditions[◇1].

Since no analytic profile for the initial scalar field is known, we define the γ factor of the colliding bubble walls using the Lorentz contraction of the wall (see Fig. 9): At the nucleation time, we have the bounce configuration along x direction, which has not yet reached the potential minimum. The scalar field reaches the minimum after some time ($\sim$ (typical potential mass scale)$^{-1}$), which we denote $t_{\gamma=1}$. We define $d_{\gamma=1}$ as the spatial distance between the two points where the scalar field takes the minimum and the maximum at this time slice. We define d_γ as the distance between such spatial points at the time slice $t = t_\gamma$. Then we define the γ factor as the ratio of the two distances:

$$\gamma = \frac{d_{\gamma=1}}{d_\gamma}. \tag{3.18}$$

For the hierarchical potential we numerically find $t_{\gamma=1} - t_n \simeq 3.83/m$. In the simulation, we identify $t_{\rm coll}$ as t_γ for a given value of γ. For the spatial discretization we use $100\gamma^2$ points for $0 < x < x_{\rm coll}$.

Fig. 10 displays the time evolution for $\gamma = 5$, 10, and 20 from top to bottom, respectively. The left panels are the value of ϕ, while the right panels are the time evolution at the collision point $\phi(t, x = x_{\rm coll})$. In the right panels the blue lines are the actual evolution in

[◇1] The details of the setup are as follows. The system size is taken to be $x_{\rm coll} \equiv (t_{\rm coll} - t_n) + 5/\gamma/m$, and we evolve the system from $t = t_{\rm coll}$ to $t = t_{\rm coll} + x_{\rm coll} \equiv t_{\rm end}$ with reflecting boundary conditions at $x = x_{\rm coll}$. The scalar configuration is taken as

$$\phi(t,x) = \begin{cases} v\left[1 - \dfrac{2J_1\left(m\sqrt{(t-t_n)^2 - x^2}\right)}{m\sqrt{(t-t_n)^2-x^2}}\right] & (0 < x < t - t_n), \\ v\,e^{-m^2\gamma^2(x-(t-t_n))^2}\left[-1 + \dfrac{2J_1\left(m\sqrt{(t-t_n)^2 - (2(t-t_n)-x)^2}\right)}{m\sqrt{(t-t_n)^2-(2(t-t_n)-x)^2}}\right] & (t - t_n < x), \end{cases}$$

in order to ensure $\partial_t\phi(t,x)|_{t=t_{\rm coll},x=x_{\rm coll}} \simeq 0$. The initial conditions are given by $\phi(t,x)|_{t=t_{\rm coll}}$ and $\partial_t\phi(t,x)|_{t=t_{\rm coll}}$.

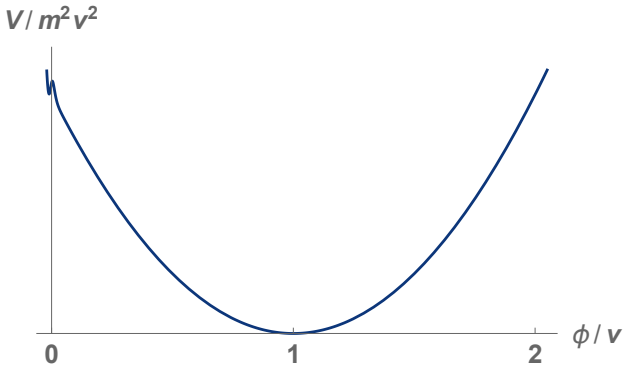

Figure 8: Potential shape of the hierarchical model.

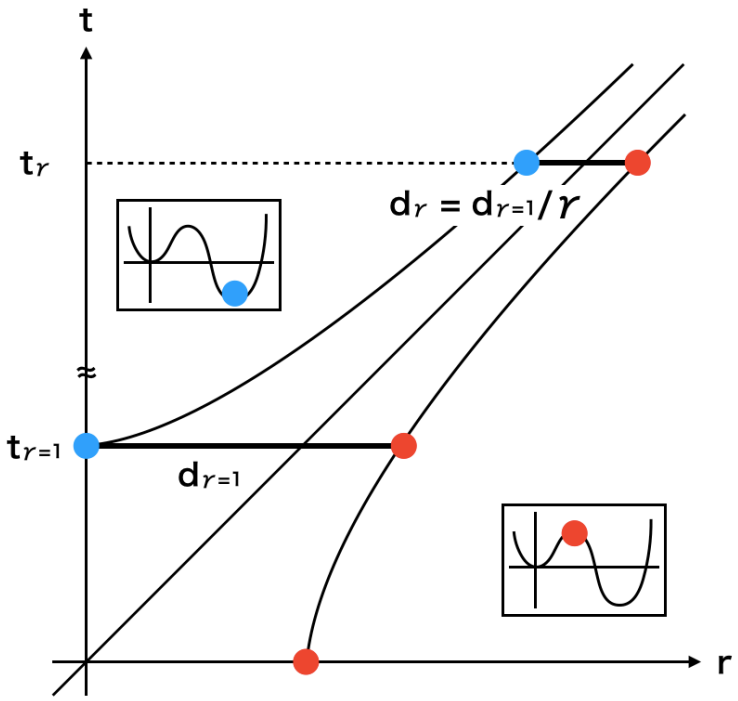

Figure 9: Definition of the wall γ factor in this paper.

our simulation, while the red lines are the prediction from the trapping equation, Eq. (2.3) (which reduces to $\phi \simeq v\,[1 + J_0(m(t - t_{\rm offset}))]$ with $t_{\rm offset} = (3.83 + 5)/\gamma/m$). In the offset, the contribution $3.83/\gamma/m$ comes from t_γ as seen in Fig. 9 and the contribution $5/\gamma/m$ comes from the offset between the collision and the initial time. We see that the prediction nicely matches the actual evolution for large γ.

3.5 Toy model 4: Simple quartic potential

Next, we consider a more realistic potential, namely

$$V = av^2\phi^2 - (2a + 4)\,v\,\phi^3 + (a + 3)\phi^4, \tag{3.19}$$

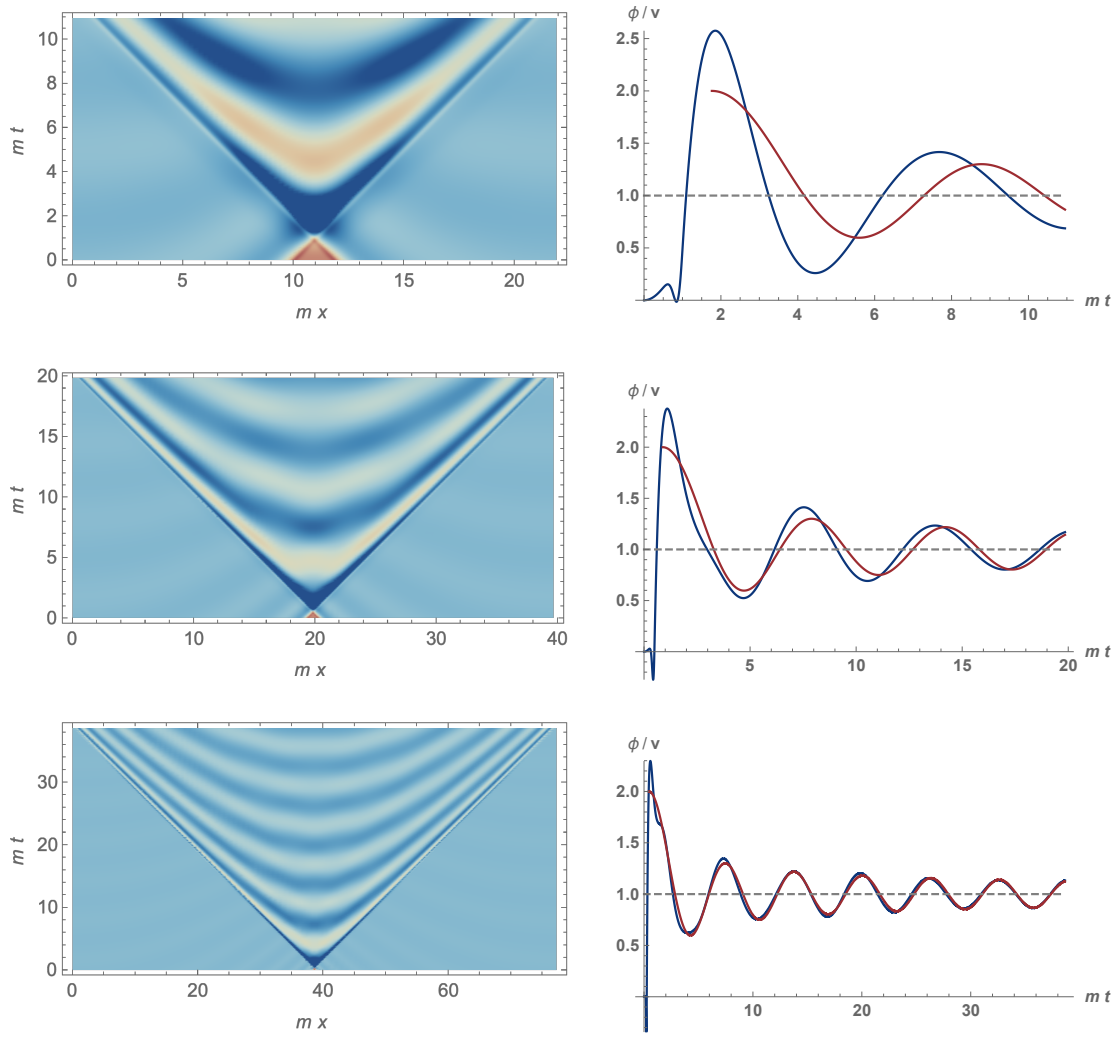

Figure 10: Hierarchical potential. **Left side:** Time evolution of ϕ for $\gamma = 5, 10$, and 20 from top to bottom. **Right side:** Time evolution of $\phi(t, x = x_{\text{coll}})$ for $\gamma = 5, 10$, and 20 from top to bottom. (Blue) Numerical evolution. (Red) Prediction from Eq. (2.3).

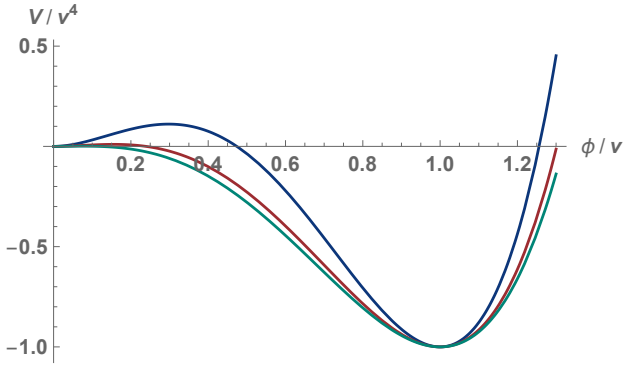

Figure 11: Quartic potential for $\epsilon = 0.1$ (blue), 0.01 (red), and 0.001 (green).

where the coefficients are chosen so that $V(v) = -v^4$ becomes a local minimum. This potential takes a local maximum at $\phi/v = a/(2a+6)$. We also define the degeneracy parameter ϵ as

$$\epsilon = \frac{(\text{barrier height}) - (\text{false vacuum height})}{(\text{barrier height}) - (\text{true vacuum height})} = \frac{a^3(a+4)}{a^3(a+4) + 16(a+3)^3}. \tag{3.20}$$

The smaller ϵ is, the smaller the false vacuum trapping becomes. In Fig. 11 we plot the potential for $\epsilon = 0.1$, 0.01, and 0.001. The trapping equation (2.3) predicts that ϕ is trapped at the false vacuum for $\epsilon \gtrsim \epsilon_{\rm th} \simeq 0.214$.

For the numerical simulation we use the same definition for the γ factor as in Fig. 9, and identify $t_{\rm coll}$ to be t_γ for a given value of γ. We use $50\gamma \times v x_{\rm coll}$ or $25\gamma \times v x_{\rm coll}$ (both $\propto \gamma^2$) points for the spatial discretization for $\gamma \leq 30$ or $\gamma > 30$, respectively.

In Fig. 12 we plot the time evolution of ϕ (left panels) and $\phi(t, x = x_{\rm coll})$ (right panels) for $\gamma = 40$ and $\epsilon = 0.5$, 0.1, and 0.05 from top to bottom. The blue (red) regions in the left panels correspond to the true (false) vacua, while the blue (red) lines in the right panels are the actual (predicted) time evolution. As predicted by Eq. (2.3), ϕ is trapped at the false vacuum soon after collision for $\epsilon = 0.5$, while it escapes for other values of ϵ.

Fig. 13 is the result of our parameter scan. The blue (red) points are the parameter values where ϕ escapes from (is trapped at) the false vacuum[◇2]. The prediction of the trapping equation $\epsilon \gtrsim \epsilon_{\rm th} \simeq 0.214$ is indicated by the green line. We see that the boundary between the blue and red points approaches the green line in the large γ limit.

3.6 Toy model 5: Quartic Z_2 potential

Finally, we consider a potential similar to the previous one but modified to have Z_2 symmetry:

$$V = av^2 |\phi|^2 - (2a+4)\, v\, |\phi|^3 + (a+3)|\phi|^4. \tag{3.21}$$

[◇2] The criterion for trapping is as follows. The 'energy' at the collision point $\left[(\partial_t\phi)^2/2 + V(\phi)\right]_{x=x_{\rm coll}}$ decreases after collision. We numerically calculate the time when it drops to the value of the barrier height $\left[(\partial_t\phi)^2/2 + V(\phi)\right]_{x=x_{\rm coll}} = V(\phi/v = a/(2a+6))$, and see whether ϕ is in the false or true vacuum side. We use the same criterion for the quartic Z_2 potential as well.

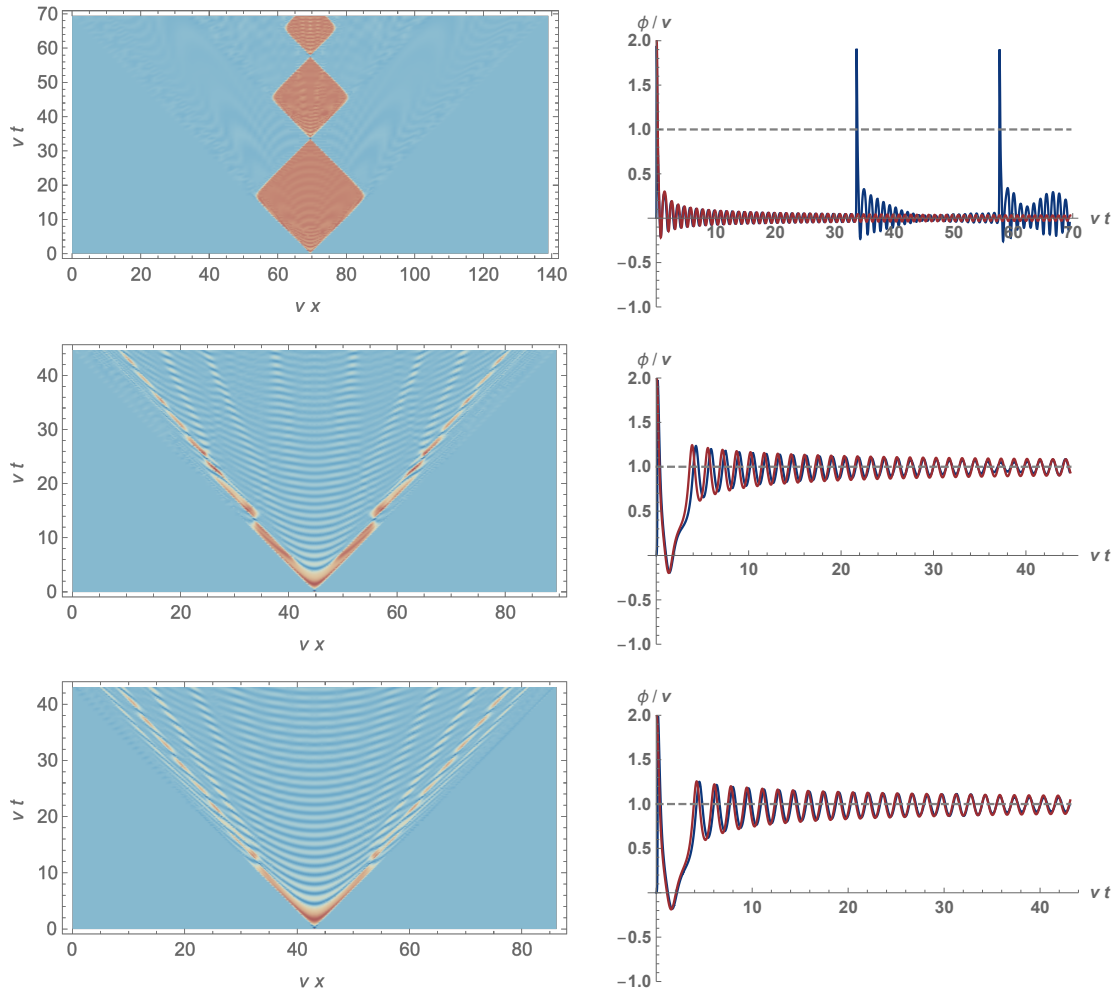

Figure 12: Simple quartic potential. **Left side:** Density plot of ϕ for $\epsilon = 0.5$, 0.1, and 0.05 and $\gamma = 40$ from top to bottom. Note that false-vacuum trapping is predicted from Eq. (2.3) for $\epsilon = 0.5$. **Right side:** Time evolution of $\phi(t, x = x_{\rm coll})$ for the parameter choice in the left panels.

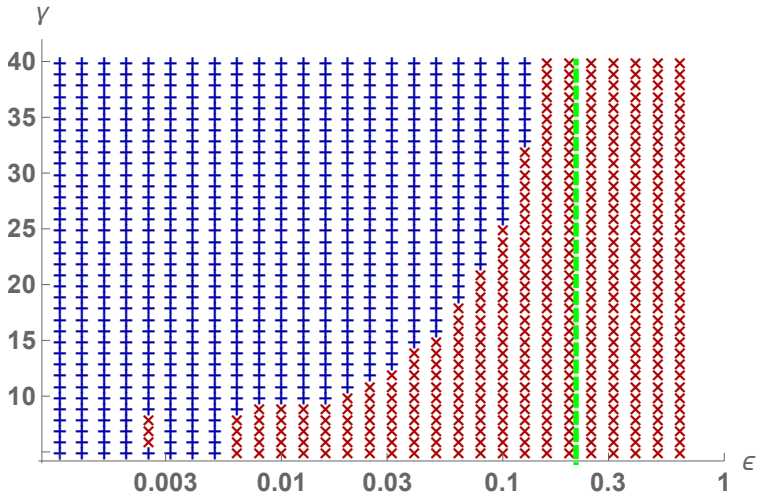

Figure 13: Simple quartic potential. The blue and red points indicate that ϕ is trapped at the true and false vacua, respectively. The green line is the threshold value $\epsilon_{\rm th} \simeq 0.214$ predicted by Eq. (2.3).

The potential is plotted in Fig. 14. The degeneracy parameter ϵ is defined in the same way as before. This setup is not realistic in that a domain wall forms after different-sign configurations collide with each other, so we study it as a toy model. In the following we make two same-sign positive configurations collide from opposite directions. The prediction from Eq. (2.3) is that ϕ is trapped at the negative (opposite) vacuum for $\epsilon < \epsilon_{\rm th}$ with $\epsilon_{\rm th} \simeq 0.867$, while it settles down to the symmetric one (vanishing VEV) for $\epsilon > \epsilon_{\rm th}$. There are no parameter values where ϕ settles down to the positive vacuum. This means that the scalar field is likely to be trapped at the opposite vacuum unless the vacua are almost degenerate. Fig. 15 is the result of numerical simulation. The red and green markers mean that ϕ is trapped in the zero and negative vacua, respectively, while the green line is the prediction of the trapping equation (2.3). As indicated from this equation, the scalar field is never trapped at the positive vacuum in the relativistic limit. Also, the boundary between the red and green regions approaches the green line in the relativistic limit.

4 Applications of the trapping equation

In the last section we compared the results of the trapping equation with results from $1+1$ dimensional simulations. We could firmly establish that in the limit of highly-relativistic wall velocities, the trapping equation predicts the correct behavior of the scalar field not only qualitatively but also quantitatively quite well.

In this section we will use the trapping equation to study more complicated setups, in particular setups with several scalar fields. In this case, lattice simulations might still be possible but solving the trapping equation is almost trivial. We discuss trapping for scalar fields with a $U(1)$ and $SU(2)$ global symmetry. As scalar potential, we use the quartic Z_2 potential in Sec. 3:

$$V(|\phi|) = av^2\,|\phi|^2 - (2a+4)\,v\,|\phi|^3 + (a+3)|\phi|^4. \tag{4.22}$$

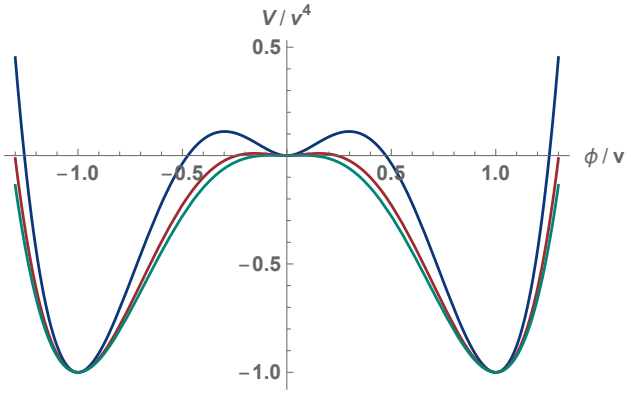

Figure 14: Quartic Z_2 potential V for $\epsilon = 0.1$ (blue), 0.01 (red), and 0.001 (green).

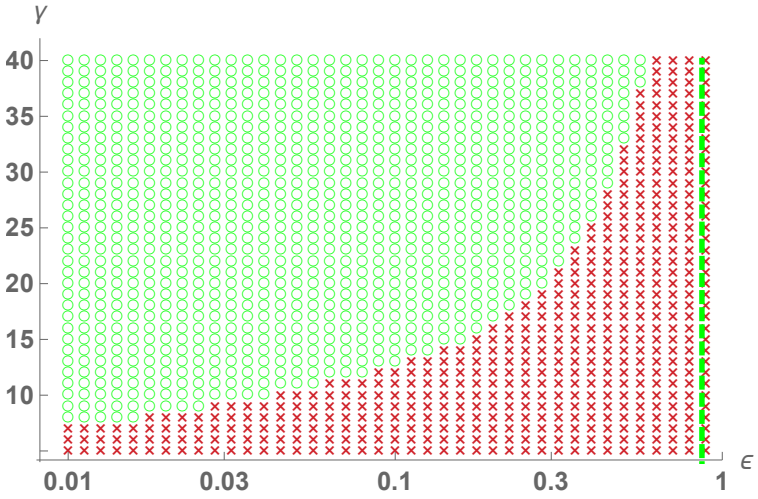

Figure 15: Quartic Z_2 potential. The red and green points indicate that ϕ is trapped at the symmetric and negative vacua, respectively. The green line is the threshold value $\epsilon_{\rm th} \simeq 0.867$ predicted by Eq. (2.3).

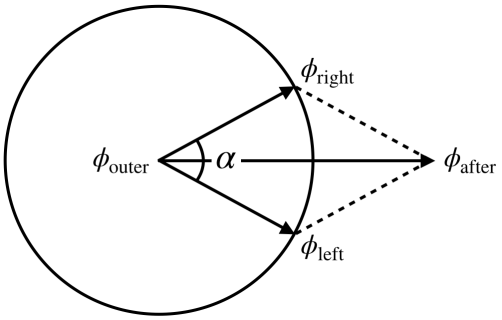

Figure 16: Opening angle α for the $U(1)$ case. The $SU(2)$ case is analogous.

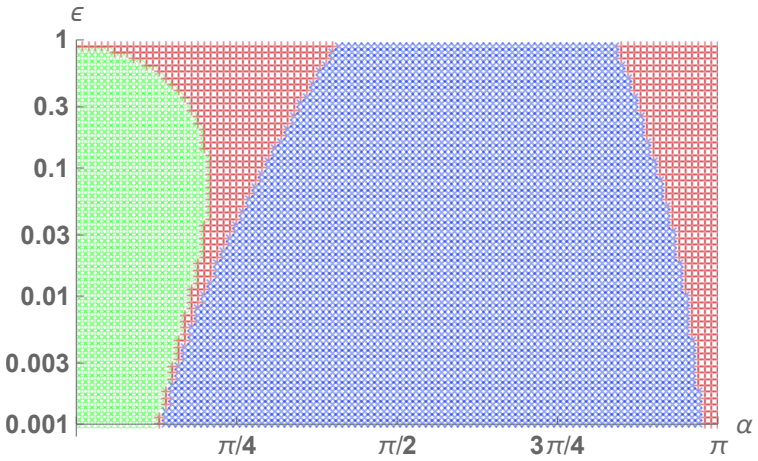

Figure 17: Prediction of the trapping equation (2.3) with the initial condition (4.23) for $U(1)$ or $SU(2)$ breaking potentials. The blue, red, and green regions correspond to $\phi = +1$, 0, and -1 for $s \to \infty$.

In both cases the collision of two solitons is parametrized by the opening angle α between the two configurations. Correspondingly, the initial condition for the trapping equation (2.3) is modified to

$$|\phi_{\text{after}} - \phi_{\text{outer}}| = |\phi_{\text{left}} + \phi_{\text{right}} - 2\phi_{\text{outer}}| = 2\,v\,\cos\left(\frac{\alpha}{2}\right), \tag{4.23}$$

where ϕ_{inner} and ϕ_{outer} are the value of ϕ in the broken and symmetric phases, respectively (see Fig. 16). The case $\alpha = 0$ then corresponds to the case studied in the last section while $\alpha = \pi$ corresponds to the collision of the two scalar walls with opposite direction in the $U(1)$ or $SU(2)$ symmetry space. In the following we take ϕ_{after} to be real and positive without loss of generality.

Fig. 17 displays the results of the trapping equation (2.3) with the initial condition (4.23). The blue, red, and green regions denote the regions where ϕ is trapped at the positive, zero, and negative (opposite) vacua, respectively. As the false vacuum trapping becomes weaker ($\epsilon \to 0$), the scalar field becomes less likely to be trapped at the false vacuum.

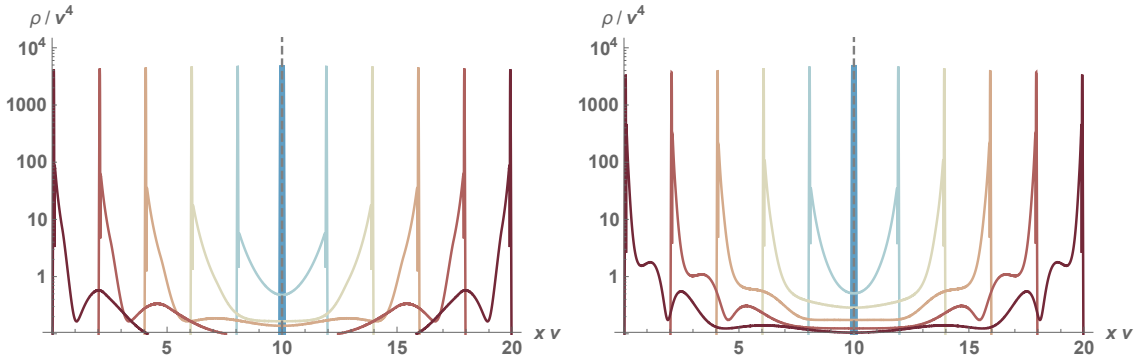

Figure 18: Modified Z_2: Time evolution of ρ for $\lambda = 0.1$ (left) and 0.3 (right) with the γ factor of 100. The system evolves from the blue lines to the red lines. These plots correspond to the parameter choice of Fig. 6. The collision occurs at $x \simeq 10/v$, where we impose reflecting boundary conditions.

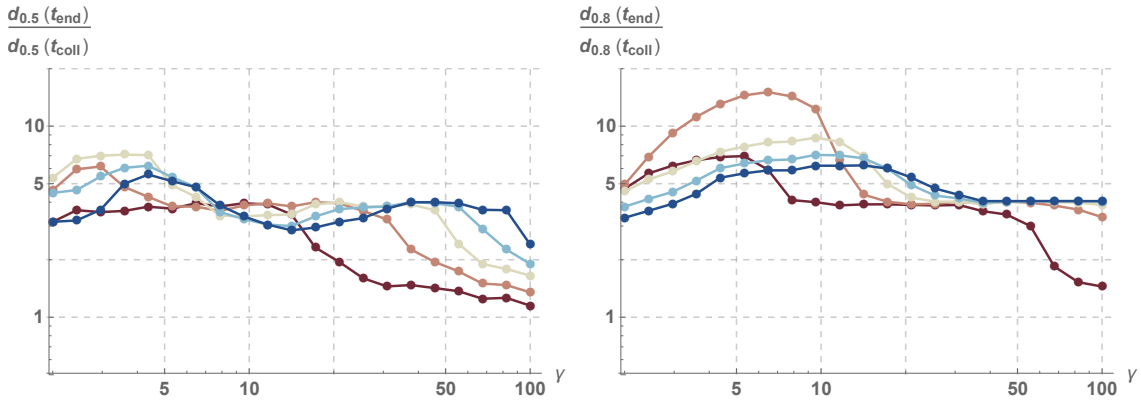

Figure 19: Modified Z_2: Thickness ratio $d_{0.5}(t_{\rm end})/d_{0.5}(t_{\rm coll})$ (left) and $d_{0.8}(t_{\rm end})/d_{0.8}(t_{\rm coll})$ (right) for $\lambda = 0.1$, 0.2, 0.3, 0.4, and 0.5 from the blue to the red lines.

5 Energy dynamics after collisions

Finally we discuss the energy dynamics after the collision. This is important because the energy distribution determines observable signatures like the GW spectrum. Indeed, the GW spectrum takes quite different forms when the scalar field instantly lose energy at the collision point [6,35,36] and when energy propagates even after collisions [37,38]. Therefore, our main interest lies in the degree of energy localization. For later purpose let us first define d_R as follows:

$$d_R \equiv \text{minimum value of the spatial interval} \\ \text{in which fraction } R \text{ of the total energy is localized.} \tag{5.24}$$

For example, $d_{0.5}$ and $d_{0.8}$ respectively mean that we can find $d_{0.5}$ and $d_{0.8}$ intervals in which 50% and 80% of the total energy is localized. In the following we present the ratio $d_R(t = t_{\rm end})/d_R(t = t_{\rm coll})$, which parametrizes the degree of wall thickening during evolution from $t_{\rm coll}$ to $t_{\rm end}$.

Modified Z_2: As a first example, consider the modified Z_2 potential in Sec. 3.2. The time evolution of the energy density ρ is displayed in Fig. 18 for $\lambda = 0.1$ (left) and 0.3 (right). The γ factor is taken to be 100. Reflecting boundary conditions are imposed at $x \simeq 10/v$, and the system evolves from the blue to the red lines. Note that these parameters are the same as Fig. 6. The left panel corresponds to the case where the scalar field stays at the positive vacuum, while in the right panel it bounces back to the negative vacuum. We see that in both cases the energy is localized at the wall front even in the last time slice (the outermost profiles).

In Fig. 19 we plot the ratio $d_{0.5}(t_{\rm end})/d_{0.5}(t_{\rm coll})$ (left) and $d_{0.8}(t_{\rm end})/d_{0.8}(t_{\rm coll})$ (right). For any value of λ, the thickness ratio keeps $\mathcal{O}(1)$ values or gradually decreases as γ increases. Note that the simulation time corresponds to the typical bubble size in a realistic situation. Since the initial wall thickness decreases as γ^{-1}, this means that the wall thickness after propagating over a distance comparable to bubble radius also decreases as γ^{-1}, regardless of whether ϕ bounces back to the old phase or not.

Hierarchical potential: Next let us discuss the hierarchical potential from Sec. 3.4. In Fig. 20 we plot the time evolution of the energy density ρ for $\gamma = 5$ (left) and 20 (right). Just as in the previous example, the energy localization is still strong even in the last time slice.

In Fig. 21 we show the thickness ratio $d_{0.5}(t = t_{\rm end})/d_{0.5}(t = t_{\rm coll})$ (blue) and $d_{0.8}(t = t_{\rm end})/d_{0.8}(t = t_{\rm coll})$ (red). We see that the thickness ratios approach $\mathcal{O}(1)$ values as γ increases. Again, since the simulation time corresponds to the typical bubble size in a realistic situation, we expect that the wall thickness remains to be (particle physics scale)$^{-1}$ even after the scalar field propagates over the typical bubble size.

Quartic potential: Let us finally study the quartic potential in Sec. 3.5. In this case the behavior of the scalar field is much more complicated than the previous two examples. We take two parameter points $\epsilon = 0.5$ (Fig. 22) and 0.05 (Figs. 23 and 24). The trapping equation (2.3) predicts that the scalar field is trapped at (escapes from) the false vacuum for the former (latter) potential at the initial stage.

In Fig. 22 we show the case with a sizable barrier between the two phases ($\epsilon = 0.5$). The left panel (the same as the top-right panel of Fig. 12) shows the time evolution of ϕ, while the right panel is the energy density distribution at $t = t_{\rm end}$. The γ factor is taken to be 40. We see from the left panel that the scalar field is indeed trapped in the false vacuum as Eq. (2.3) predicts. We also see several collisions at $vt \simeq 0$, 34, and 58 caused by the trapping. Since the scalar field is again trapped in the false vacuum, the large pressure across the wall decelerates the wall and then accelerates it again for the subsequent collision. These multiple collisions result in the energy distribution in the right panel at the simulation end. The three peaks (from outside to inside) come from the first, second and third collisions, respectively, while the energy localization at the center is the effect of trapping still continuing at the simulation end. Interestingly, the outermost peak does not dominate the energy of the system: it carries only 0.241 of the total energy, and this fraction does not change significantly even if γ increases. Indeed it takes 0.245 and 0.246 for $\gamma = 50$ and 60, respectively. In addition, the distance between the outermost and inner peaks is stable against the change in γ, since it is determined by the condition "(energy released until just before collision) $\simeq$ (energy stored in the false vacuum trapping)". Therefore, we

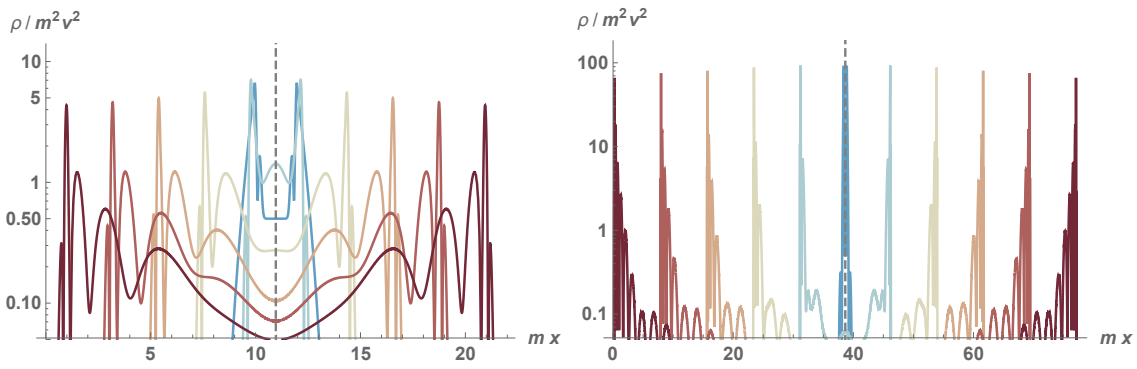

Figure 20: Hierarchical potential: Time evolution of ρ for $\gamma = 5$ (left) and 20 (right). The collision occurs at the center, where we impose reflecting boundary conditions, and the system evolves from the blue to the red lines.

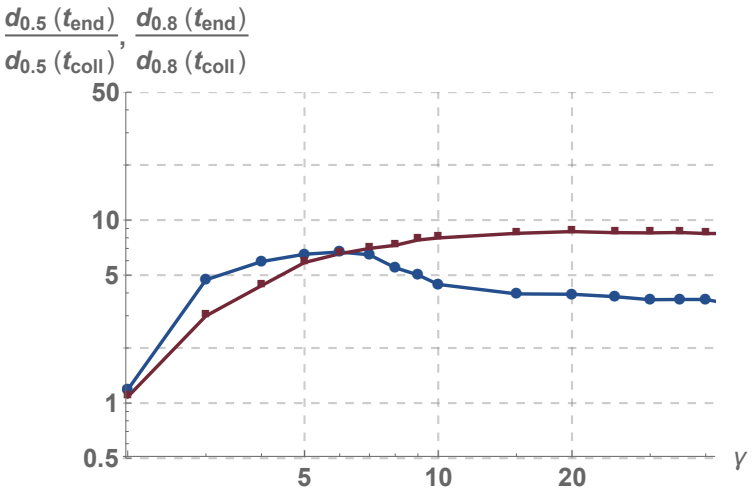

Figure 21: Thickness ratio $d_{0.5}(t = t_{\text{end}})/d_{0.5}(t = t_{\text{coll}})$ (blue) and $d_{0.8}(t = t_{\text{end}})/d_{0.8}(t = t_{\text{coll}})$ (red) for the hierarchical potential.

conclude that the energy does not localize at the front if trapping occurs[◇3].

In Fig. 23 we show the case with a rather small barrier ($\epsilon = 0.05$). The γ factor is taken to be the same as before, $\gamma = 40$. We see that the trapping does not occur, as Eq. (2.3) predicts. In contrast to Fig. 22, the outermost peaks are the highest ones in this case. The subsequent peaks carry a non-negligible fraction of the total energy, but they merge with the outermost ones in the large γ limit. Fig. 24 confirms this statement: the left and right panels show the energy localization for $\gamma = 50$ and 60 with the same value of ϵ, respectively. We clearly see that subdominant peaks merge with the outermost ones. Therefore, we conclude that the energy localization and the propagation speed of the wall persist even after collisions if trapping does not occur.

In summary, there are several cases to consider for the energy distribution. If the false and true vacua are degenerate, the energy localization is still strong even after the walls propagate over a distance of order bubble radius after collision. This holds true regardless of whether the scalar field bounces back or not (modified Z_2), since the bubble wall does not decelerate after collision.

When the two vacua are not degenerate, the energy distribution depends on the dynamics of the scalar field. In case the false vacuum trapping does not occur, the energy localization is still much thinner than the bubble size (this has been the case for the hierarchical potential and the quartic potential with $\epsilon = 0.05$). If the false vacuum trapping occurs after collision, the scalar field feels a decelerating pressure and the energy gets dispersed from the relativistic front (as seen for the quartic potential with $\epsilon = 0.5$). The trapping equation (2.3) is hence a useful tool in determining the energy distribution after bubble collisions.

6 Conclusions

In this paper we studied scalar field bubble collisions in first-order phase transitions in the relativistic regime. It is of great importance to understand the scalar field dynamics and the energy distribution in this case, since the shape of the GW spectrum differs significantly depending on whether the bubble walls instantly lose energy at the collision point or the energy propagates much further after collision.

We proposed a 'trapping equation' which describes the behavior of bubbles at the initial stage after the collision. The equation can be used to determine whether or not the scalar field bounces back and becomes trapped in the false vacuum. We extensively tested the validity of the trapping equation in a variety of setups in Sec. 3 and compared with scalar field simulations. We also discussed the implication of the trapping equation to $U(1)$ or $SU(2)$ breaking transitions in Sec. 4 where scalar field simulations are more elaborate.

The false vacuum trapping has a huge impact on the resulting GW spectrum, since it leads to a decelerating pressure on the propagating scalar field and therefore changes the extent of energy penetration after collision [39]. Ultimately, the 'trapping equation' determines which mechanism of GW production prevails after the phase transition: The so-called envelope approximation [5, 6, 35, 36] or the bulk flow model [37, 38].

[◇3] However, note two things: (1) The distance between the outermost and inner peaks is $\mathcal{O}(0.1) \times$ (bubble radius), which will not change significantly even in $3+1$ dimensional collisions. (2) Both peaks propagate at relativistic speeds. These mean that, after the energy peaks propagate over a distance much longer than the bubble radius at collisions, their distance is much shorter than the radius of the bubble-like structures. Therefore, the IR structure pointed out in Ref. [37] may appear in the GW spectrum.

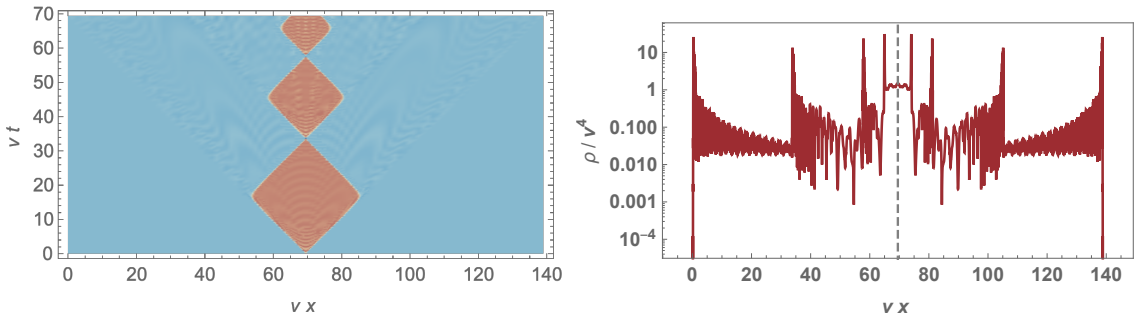

Figure 22: Time evolution of ϕ (left) and the energy density at the simulation end $\rho(t = t_{\rm end})$ (right) for the quartic potential with $\epsilon = 0.5$ and $\gamma = 40$. The collision occurs at the position of the dashed line in the right panel. The trapping equation (2.3) predicts that ϕ is trapped at the false vacuum at the initial stage.

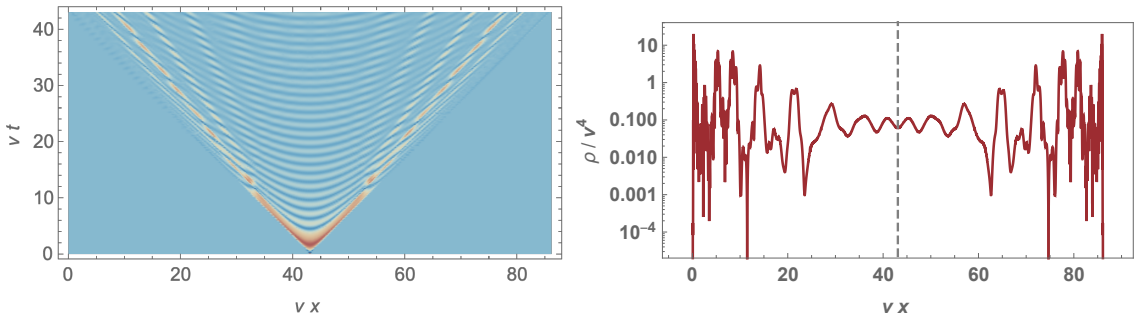

Figure 23: The same as Fig. 22 except that $\epsilon = 0.05$ and $\gamma = 40$. The trapping equation (2.3) predicts that ϕ escapes from the false vacuum.

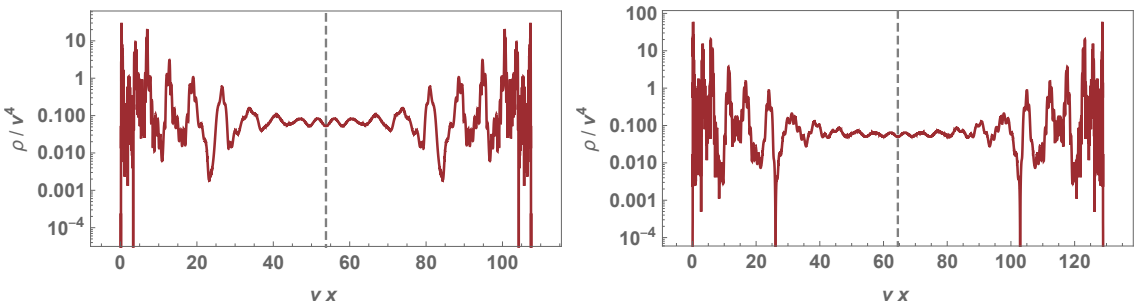

Figure 24: How the right panel of Fig. 23 changes for different values of γ. The value of γ is chosen to be 50 and 60 for the left and right panels, respectively. The inner peaks merge with the outermost peaks as γ increases.

Acknowledgment

The work of RJ was supported by Grants-in-Aid for JSPS Overseas Research Fellow (No. 201960698). This work is supported by the Deutsche Forschungsgemeinschaft under Germanys Excellence Strategy – EXC 2121 „Quantum Universe“ – 390833306.

References

[1] V. A. Kuzmin, V. A. Rubakov, and M. E. Shaposhnikov, "On the Anomalous Electroweak Baryon Number Nonconservation in the Early Universe," *Phys. Lett.* **155B** (1985) 36.

[2] E. Witten, "Cosmic Separation of Phases," *Phys. Rev.* **D30** (1984) 272–285.

[3] C. J. Hogan, "Gravitational radiation from cosmological phase transitions," *Mon. Not. Roy. Astron. Soc.* **218** (1986) 629–636.

[4] A. Kosowsky, M. S. Turner, and R. Watkins, "Gravitational radiation from colliding vacuum bubbles," *Phys. Rev.* **D45** (1992) 4514–4535.

[5] A. Kosowsky, M. S. Turner, and R. Watkins, "Gravitational waves from first order cosmological phase transitions," *Phys. Rev. Lett.* **69** (1992) 2026–2029.

[6] A. Kosowsky and M. S. Turner, "Gravitational radiation from colliding vacuum bubbles: envelope approximation to many bubble collisions," *Phys. Rev.* **D47** (1993) 4372–4391, arXiv:astro-ph/9211004 [astro-ph].

[7] M. Kamionkowski, A. Kosowsky, and M. S. Turner, "Gravitational radiation from first order phase transitions," *Phys. Rev.* **D49** (1994) 2837–2851, arXiv:astro-ph/9310044 [astro-ph].

[8] T. Vachaspati, "Magnetic fields from cosmological phase transitions," *Phys. Lett.* **B265** (1991) 258–261.

[9] D. Bodeker and G. D. Moore, "Can electroweak bubble walls run away?," *JCAP* **0905** (2009) 009, arXiv:0903.4099 [hep-ph].

[10] D. Bodeker and G. D. Moore, "Electroweak Bubble Wall Speed Limit," *JCAP* **1705** no. 05, (2017) 025, arXiv:1703.08215 [hep-ph].

[11] L. Randall and G. Servant, "Gravitational waves from warped spacetime," *JHEP* **05** (2007) 054, arXiv:hep-ph/0607158 [hep-ph].

[12] J. R. Espinosa, T. Konstandin, J. M. No, and M. Quiros, "Some Cosmological Implications of Hidden Sectors," *Phys. Rev.* **D78** (2008) 123528, arXiv:0809.3215 [hep-ph].

[13] T. Konstandin and G. Servant, "Cosmological Consequences of Nearly Conformal Dynamics at the TeV scale," *JCAP* **1112** (2011) 009, arXiv:1104.4791 [hep-ph].

[14] T. Hambye and A. Strumia, "Dynamical generation of the weak and Dark Matter scale," *Phys. Rev.* **D88** (2013) 055022, arXiv:1306.2329 [hep-ph].

[15] J. Jaeckel, V. V. Khoze, and M. Spannowsky, "Hearing the signal of dark sectors with gravitational wave detectors," *Phys. Rev.* **D94** no. 10, (2016) 103519, arXiv:1602.03901 [hep-ph].

[16] R. Jinno and M. Takimoto, "Probing a classically conformal B-L model with gravitational waves," *Phys. Rev.* **D95** no. 1, (2017) 015020, arXiv:1604.05035 [hep-ph].

[17] L. Marzola, A. Racioppi, and V. Vaskonen, "Phase transition and gravitational wave phenomenology of scalar conformal extensions of the Standard Model," *Eur. Phys. J.* **C77** no. 7, (2017) 484, arXiv:1704.01034 [hep-ph].

[18] S. Iso, P. D. Serpico, and K. Shimada, "QCD-Electroweak first order phase transition in supercooled universe," arXiv:1704.04955 [hep-ph].

[19] C.-W. Chiang and E. Senaha, "On gauge dependence of gravitational waves from a first-order phase transition in classical scale-invariant $U(1)'$ models," *Phys. Lett.* **B774** (2017) 489–493, arXiv:1707.06765 [hep-ph].

[20] B. von Harling and G. Servant, "QCD-induced Electroweak Phase Transition," *JHEP* **01** (2018) 159, arXiv:1711.11554 [hep-ph].

[21] S. Bruggisser, B. Von Harling, O. Matsedonskyi, and G. Servant, "Baryon Asymmetry from a Composite Higgs Boson," *Phys. Rev. Lett.* **121** no. 13, (2018) 131801, arXiv:1803.08546 [hep-ph].

[22] S. Bruggisser, B. Von Harling, O. Matsedonskyi, and G. Servant, "Electroweak Phase Transition and Baryogenesis in Composite Higgs Models," *JHEP* **12** (2018) 099, arXiv:1804.07314 [hep-ph].

[23] I. Baldes and C. Garcia-Cely, "Strong gravitational radiation from a simple dark matter model," arXiv:1809.01198 [hep-ph].

[24] K. Hashino, R. Jinno, M. Kakizaki, S. Kanemura, T. Takahashi, and M. Takimoto, "Fingerprinting models of first-order phase transitions by the synergy between collider and gravitational-wave experiments," arXiv:1809.04994 [hep-ph].

[25] T. Prokopec, J. Rezacek, and B. wieewska, "Gravitational waves from conformal symmetry breaking," *JCAP* **1902** no. 02, (2019) 009, arXiv:1809.11129 [hep-ph].

[26] V. Brdar, A. J. Helmboldt, and J. Kubo, "Gravitational Waves from First-Order Phase Transitions: LIGO as a Window to Unexplored Seesaw Scales," *JCAP* **1902** (2019) 021, arXiv:1810.12306 [hep-ph].

[27] C. Marzo, L. Marzola, and V. Vaskonen, "Phase transition and vacuum stability in the classically conformal B-L model," arXiv:1811.11169 [hep-ph].

[28] P. Baratella, A. Pomarol, and F. Rompineve, "The Supercooled Universe," *JHEP* **03** (2019) 100, arXiv:1812.06996 [hep-ph].

[29] M. Fairbairn, E. Hardy, and A. Wickens, "Hearing without seeing: gravitational waves from hot and cold hidden sectors," arXiv:1901.11038 [hep-ph].

[30] H. L. Child and J. T. Giblin, Jr., "Gravitational Radiation from First-Order Phase Transitions," *JCAP* **1210** (2012) 001, arXiv:1207.6408 [astro-ph.CO].

[31] J. Braden, J. R. Bond, and L. Mersini-Houghton, "Cosmic bubble and domain wall instabilities I: parametric amplification of linear fluctuations," *JCAP* **1503** no. 03, (2015) 007, arXiv:1412.5591 [hep-th].

[32] J. Braden, J. R. Bond, and L. Mersini-Houghton, "Cosmic bubble and domain wall instabilities II: Fracturing of colliding walls," *JCAP* **1508** no. 08, (2015) 048, arXiv:1505.01857 [hep-th].

[33] J. R. Bond, J. Braden, and L. Mersini-Houghton, "Cosmic bubble and domain wall instabilities III: The role of oscillons in three-dimensional bubble collisions," *JCAP* **1509** no. 09, (2015) 004, arXiv:1505.02162 [astro-ph.CO].

[34] D. Cutting, M. Hindmarsh, and D. J. Weir, "Gravitational waves from vacuum first-order phase transitions: from the envelope to the lattice," *Phys. Rev.* **D97** no. 12, (2018) 123513, arXiv:1802.05712 [astro-ph.CO].

[35] S. J. Huber and T. Konstandin, "Gravitational Wave Production by Collisions: More Bubbles," *JCAP* **0809** (2008) 022, arXiv:0806.1828 [hep-ph].

[36] R. Jinno and M. Takimoto, "Gravitational waves from bubble collisions: An analytic derivation," *Phys. Rev.* **D95** no. 2, (2017) 024009, arXiv:1605.01403 [astro-ph.CO].

[37] R. Jinno and M. Takimoto, "Gravitational waves from bubble dynamics: Beyond the Envelope," *JCAP* **1901** (2019) 060, arXiv:1707.03111 [hep-ph].

[38] T. Konstandin, "Gravitational radiation from a bulk flow model," *JCAP* **1803** no. 03, (2018) 047, arXiv:1712.06869 [astro-ph.CO].

[39] T. Konstandin and G. Servant, "Natural Cold Baryogenesis from Strongly Interacting Electroweak Symmetry Breaking," *JCAP* **1107** (2011) 024, arXiv:1104.4793 [hep-ph].